Energy Conversion and Management 342 (2025) 120131

Contents lists available at ScienceDirect

Energy Conversion and Management

journal homepage: www.elsevier.com/locate/enconman

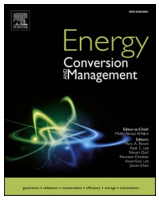

Research Paper

Thermal performance and dynamic response assessment of an industrial molten salts based power-to-heat system

Silvia Trevisan [a,*], Sharat Pathi [b], James Brown [b], Bjarke Buchbjerg [b], Andres Barros Borrero [b], Rafael Guedez [a]

[a] Department of Energy Technology, KTH Royal Institute of Technology, 100 44 Stockholm, Sweden
[b] KYOTO Group AS, 1366 Lysaker, Norway

A B S T R A C T

Flexible power-to-heat systems that incorporate thermal energy storage are key technologies to decarbonize industry. This study examines the thermal and dynamic performance of a power-to-heat MW-scale pilot plant that integrates molten salt electric heating and thermal energy storage to generate steam on demand. Operational data collected under nearly design and off-design conditions are discussed. The dynamic performance of the electric heater unit is also assessed and presented in detail, including time constants and ramping up efficiencies. The results confirm the ability of the system to deliver reliable heat on demand whilst simultaneously being able to provide grid-flexibility. Round-trip thermal efficiencies above 94 % were obtained when operating near design conditions. Thermal losses of approximately 0.5 and 2.3 °C/h were recorded for the cold and hot tanks respectively during standstill periods. Thermal losses are negatively affected by the small scale of the investigated facility and should be expected to decrease inversely proportional to the anticipated increase in size of tanks in full scale commercial installations. The ability of the electric heater to ramp up its electric power consumption from 0 to 5 MWe in 5 s is demonstrated, showing the capacity of the system of participating in frequency regulation markets. The electric heater is characterized by thermal time constants below 500 s and ramping up thermal efficiency of 80 %. This work provides the ground for performance validation of molten salt based flexible power-to-heat systems, reaffirming their potential as industry heat decarbonization assets, and highlighting opportunities for improvement.

1. Introduction

The industrial sector is a major emitter of greenhouse gases [1], and one of the main barriers and challenges in achieving the worldwide emission reduction targets [2]. Nowadays, about 48 % of the overall energy demand is consumed as heat, and 22 % of the overall energy demand is required as heat by the industrial sector. Globally, about 87 % of the industrial heat is produced via fossil sources, generating about 30 % of the whole global carbon emissions [3]. Such industrial heat demand is also foreseen to increase by 16 % by 2028 [4]. To attain the needed decarbonization of the industrial sector, technically efficient and cost-effective solutions are required [5]. Electrification of heat and flexible power-to-heat solutions including thermal energy storage (TES) are expected to represent a key technology for deep decarbonization of the industrial sector [6]. TES integrated power-to-heat technologies can not only offer opportunities for direct heat decarbonization but also, among other: load shifting, increased renewables penetration, heat and power sector coupling, as well as grid support services [7].

Indeed, TES has been found to play a crucial role in achieving and maintaining decarbonized grids, reducing renewable curtailment and improving their operation [8]. Madeddu et al. [9] estimated that 78 % of the industrial heat demand is currently electrifiable via available technologies, which would lead to a 78 % reduction of the industrial CO2 emissions. However, direct electrification without flexibility options can represent a major challenge for grid stability and effective decarbonization. Sorknæs et al. [10] highlighted that industrial electrification should be favored to attain a 100 % renewable industrial sector. To enable this shift, the authors showed that flexible units, among others heat storage, would be fundamental. Prenzel et al. [11] focused on the chemical sector and showed that the integration of molten salts based power to heat and TES systems can promote decarbonization whilst providing cost savings up to 27 % and increased system resilience. Pee et al. [12] estimated that the cement industry could be decarbonized via electricity based technologies at a cost between 60 and 250 USD (depending on the electricity price) per avoided ton of CO2 (equivalent to the range from 50 to 213 € per avoided ton of CO2 considering the average exchange rate of 2018, equal to 0.849 [13]). Peng et al. [14] proposed a TES based on electrically conductive ceramic storing up to 1100 °C that could attain the US DOE's 50 USD/MWh$_{th}$ (equivalent to a target of about 47 €/MWh$_{th}$ considering the average exchange rate of 2022, equal to 0.936 [13]). The authors [15] previously showed the

* Corresponding author.
E-mail address: trevisan@kth.se (S. Trevisan).

https://doi.org/10.1016/j.enconman.2025.120131
Received 15 January 2025; Received in revised form 18 June 2025; Accepted 26 June 2025
Available online 4 July 2025

Nomenclature

Acronyms

BMS	Battery management system
CFD	Computational fluid dynamics
CH	Charge
CHP	Combined heat and power
CO_2	Carbon dioxide
DH	District heating
DHN	District heating network
DISCH	Discharge
DOE	Department of Energy
EH	Electric heater
EMS	Energy management system
KPI	Key performance indicators
MS	Molten salts
SGS	Steam generator
TES	Thermal energy storage
US	United States
USD	United States Dollar

Symbols

c_p	Specific heat [J/(kg•K)]
E	Energy [MWh]
$\dot{m}$	Mass flow rate [kg/s]
P	Power [MW]
T	Temperature [°C]
t	Time [s]

Greek symbols

δ	Delay [s]
η	Efficiency
ρ	Density [kg/m^3]
τ	Time constant [s]

Subscripts

ch	Charge
disch	Discharge
end	End of the process (for charge and discharge)
in	Inlet
out	Outlet
ramp-up	Ramping up

techno-economic feasibility of molten salts base power-to-heat systems for industrial steam generation with levelized cost of heat between 55 and 80 €/MWh with considerable savings with respect to non-flexible electric heaters.

Considering the foreseen techno-economic potential of these solutions, more recent research focused on experimental demonstration of laboratory to small pilot scale testing units of power-to-heat systems integrating TES. Royo et al. [16] demonstrated the flexibility potential of a PCM based pillow plates TES with immersed resistance heating cartridges also showing charging efficiencies in the range 65–95 %. Xiao et al. [17] tested the charging process up to 280 °C of a lab scale latent heat TES based on binary solar, metal foam and aluminium oxide nanoparticles including an immersed 380 W resistive electric heater. The results showed potential for increments of the TES volumetric mean power by more than three times the one of pure solar salt when employing copper foams. Weiss et al. [18] presented the experimental characterization of a 225 kWh binary solar salts TES with filler material validating the exploitation of thermocline concepts employing molten salts. It should be mentioned that large scale solar salts TES are commercially employed in concentrating solar power plants (CSP) operating up to 565 °C. However, several failures have been reported typically caused by the thermo-mechanical interaction between the salts and the TES tank leading to fatigue, stress relaxation cracking, creep and buckling among others [19]. The report produced by NREL described these failures and their main link to the manufacturing process of the TES tanks, their large scale (typically with diameters larger than 30 m and height above 10 m), and the high operating temperatures above 500 °C.

As of today, electric heaters (EH) are the dominant power to heat element operated during TES charge providing system flexibility. Most research on EH for industrial TES applications has been focused on optimizing the unit design, particularly elements and baffles arrangement, to maximize the homogeneity of the temperature distribution and minimize local hot spots. Mahdi et al. [20] modelled via CFD the thermal behaviour of a 600 kW solar salts electric heater and validated this model against dynamic modelling in Dymola, achieving an error margin of about 20 %. Yang et al. [21] proposed the conceptual design and experimental validation of an eccentric micro annular channel electric heater for chloride based TES operated up to 18 kV and up to 270 thermal cycles between 400 °C and 820 °C. The numerical model was developed in ANSYS Fluent with a finite volume discretization and a realizable κ-ε model for the salts turbulent flow. Drosatos et al. [22] focused on a 7 MW_e EH for solar salts and assessed the influence of the orientation of the unit and different baffles arrangement. He et al. [23] focused on a CFD based optimization of the design of a 250 kW solar salts electric heater, showing that increasing the number of baffles and including purposely designed openings in the baffles can contribute to limiting local overheating. Of particular interest, Prenzel et al. [24,25] showed the experimental performance of two 360 kW EH units for solar salts operating up to 560 °C. The results highlighted efficiencies up to 98 % in steady state operation. However, after more than 5′000 cycles at temperatures above 500 °C cracks of the oxide layer around the EH elements were observed.

In the broader context of industrial decarbonization, the relevance of power-to-heat technologies, when coupled with storage, in supporting grid stability via provision of ancillary services has been previously highlighted [26]. However, most of the existing work displaying examples for power to heat units exploitation for ancillary services focuses on district heating and the building sector in which the thermal mass of the district heating network and buildings can be exploited [27]. Sihvonen et al. [28] also highlighted that reserve market participation, particularly frequency restoration and containment reserves, can increase the profitability of power-to-heat unit and storage by up to 29 %. However, these results are bound to the specific responsiveness of the considered power-to-heat technology and the level of flexibility offered by the storage units.

Considering the above state of the art, there is a lack of insights on the performance of full-scale (MW) power-to-heat systems including TES, going beyond small-scale laboratory set-up within controlled environment. Studies focused on large scale TES for CSP applications provide a solid ground for molten salts based solutions within the industrial decarbonization context. However, the required downscaling and modularity of the TES systems for industrial decarbonization bring novel challenges in relation to, among others, tanks design and circulation systems. Additionally, most of the research focused on solar salts applications whilst there is a lack of validated data regarding ternary salts, which have been suggested as more suitable for industrial applications [26]. When focusing on the electric heaters, most studies address design challenges via CFD studies, but they present neither the thermal and dynamic performance nor the reference data. It is important to highlight that upscaling of power-to-heat system comes with several challenges related to, among others: thermal inertia, thermal losses,

fluid management and circulation systems; which require particular attention and specific validation. The participation of power to heat units in flexibility markets have been modelled and tested in different contexts focusing on district heating applications including electric boilers and heat pumps [27,28]. However, there is a lack for data based assessment for high temperature industrial power to heat dynamic responses which might affect the applicability of these technologies in markets demanding fast activation times.

This study aims at fulfilling the identified gap by providing operational data (including charge, discharge, and simultaneous operation) and thermal performance of a MW scale (nominal operating conditions equivalent to 5 MW_e, 18 MWh_{th}, 4 MW_{th}) power-to-heat unit integrating a ternary molten salts based modular TES. The system performance is discussed for nearly design operation as well as for off-design conditions. In doing so, this work provides performance validation data, key insights and ground for further technological development. Additionally, this study presents specific thermal and dynamic performance of the EH unit, key component required to attain system's flexibility. In doing so, time constants, thermal responsiveness, and efficiency during transient operation are reported and discussed. These data are crucial for the thermal and dynamic characterization and modelling of the electric heater unit to maximize the controllability of the unit and its integration in flexible and more resilient power grids.

2. Materials and methods

This section introduces the investigated system providing some specific insights into its main components, operational strategies and integration. Additionally, the main methods exploited for the system performance assessment and relative KPIs are defined and described.

2.1. System description

Fig. 1 shows two annotated photographs of the molten salts power to heat and TES pilot installation object of this study (KYOTO's Heatcube installation at Norbis Park, Aalborg, Denmark). The installation has been inaugurated in August 2023 and since then it has been used for a comprehensive operational derisking of the unit at full industrial scale. The data and performance assessment presented in this study refer to the operation of this pilot installation. Fig. 2 provides an overview schematic layout of the power to heat and TES installation including its main components: MS pump, electric heater, MS tanks (T1 to T6), connections to SGS, valves and main instrumentation along the circulation system.

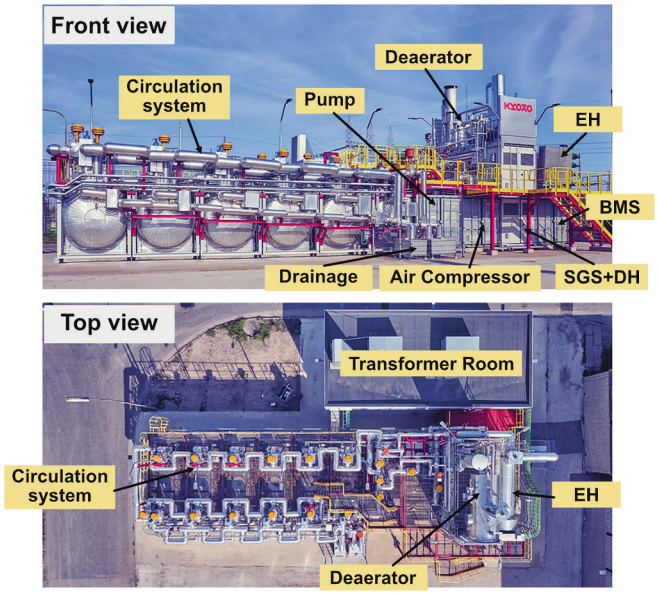

Fig. 1. Annotated photographs of the studied KYOTO's Heatcube pilot installation at Norbis Park, Aalborg, Denmark highlighting the main subcomponents.

The industrial pilot installation has six MS tanks, placed horizontally, which provides a total storage capacity of about 18 MWh. To guarantee only five tanks are filled with salts and one is empty operation (as will be explained in section 2.2 and previously discussed in [15]). The storage material is Yara MOST ternary molten salt (NaNo3, KNO3, Ca(NO3)2) [29], whose main properties are summarized in Table 1. With respect to traditional binary solar salts [30], the selected salt can operate at lower minimum temperatures providing a better fit with the process heat typical requirements and limiting the needs for thermal insulation. The tanks have a net volume of about 16 m^3 (a total volume of about 17.6 m^3), present an outer total length of 6058 mm, and total external diameter of 2050 mm. The limited dimension of the tanks has been selected to fit in standard size containers (also once insulated) and limit the need for dedicated special transport on site. However, it should be highlighted that the specific tank dimensions reflect the pilot characteristics of the site and are not considered to be optimal, particularly when considering larger scale fully commercial installation. The TES tanks have been designed, including safety factors, for maximum temperatures of 538 °C and design pressure of 1.5 barg. The full body of the tanks is made of austenitic stainless steel. The tanks are supported by a purposely designed steel-based support structure with specific profiles to limit thermal bridges. The tanks are surrounded by 100 mm layered insulation made of Pyrogel and Rockwool. The tanks include two systems for temperature control and anti-freezing, which can provide up to a total of 85 kW: a set of immersed electric heaters, and heat tracing. Three K-type thermocouples (with a typical accuracy of ±0.10 %) are installed within each tank at a depth of 300 mm, 1100 mm and 2000 mm from the top to monitor the temperature at different levels, as sketched in Fig. 3. A level sensor is also installed within each tank to monitor the salts level, which is operated between a minimum level of 200 mm (equivalent to about 5 % of the total volume) and a maximum level of 1845 mm (equivalent to about 95 % of the total volume), as sketched in Fig. 3. The main MS circulation system is sized for a design mass flow rate of 16.7 kg/s (and a maximum threshold of 19.3 kg/s) with DN80 austenitic stainless-steel pipes. An ultrasonic flow meter is installed to monitor the MS flow rate during full operation. A high temperature molten salts centrifugal pump provides the MS flow during system operation. An in-line flow MS electric heater is the main charging unit with a design power rate of 5 MW_e and design MS inlet and outlet temperatures of 220 °C and 450 °C, respectively. The electric heater is divided into 4 stages, each equipped with a dedicated power meter, to increase unit controllability all stages have a stepless control between zero and the rated power. The electric heater is monitored via 13 K-type thermocouples to monitor the temperatures of the MS flow, heater elements and vessel. The air compressor room contains a compressor able to deliver up to 12 m^3/h at 10 barg and two 2 m^3 storage. The dry and clean compressed air is used for actuation of the pneumatic valves and to facilitate the salts flow in priming and draining operation. The steam generation (SGS) and district heating (DH) connection subsystem includes primarily three different pumps (for feedwater, condensate and DH water), deaerator, steam generator, condenser, and blowdown tank. The main steam generator is a single train 4 MW_{th} water tube header coil heat exchanger in which MS is used to produce steam. The produced steam is then condensed in the plate and shell condenser by delivering heat to the main water flow from the local district heating network (DHN). Cold water enters the condenser in the range 35 °C–45 °C, hot water is produced at the condenser outlet at temperature as high as 143 °C for thermal load of 0.5 MW_{th} and at 95 °C for thermal load of 4 MW_{th}. Finally, water is delivered to the DH grid in the temperature range 75–90 °C. The connection with the DHN is equipped with a thermal power meter measuring the heat delivered to the grid, which is used for both performance monitoring as well as billing scopes. Purposely designed battery management system (BMS) and energy management system (EMS) provide the full range of control and operation to

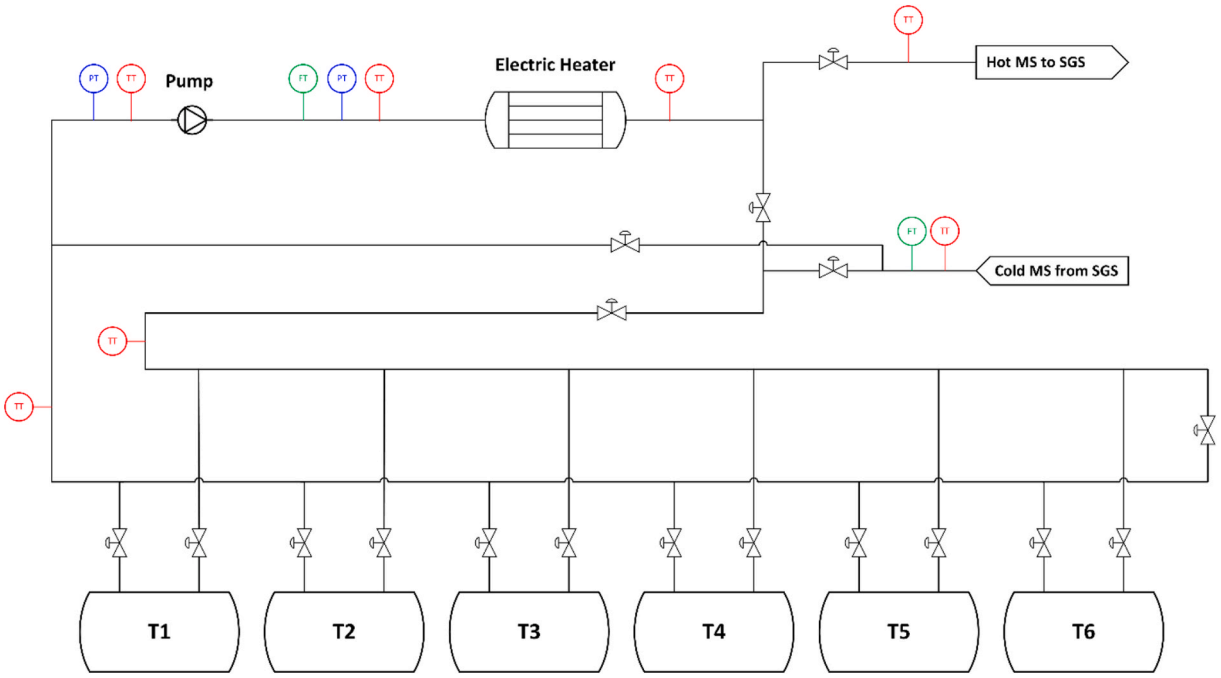

Fig. 2. Schematic layout of the pilot installation and its main components including: MS pump, electric heater, MS tanks (T1 to T6), connections to SGS, valves and main instrumentation (TT- temperature, PT – pressure, FT – flow) along the circulation system.

Table 1
Main thermo-physical properties of the considered ternary molten salts [29].

Parameter	Value	Unit
Melting temperature	131	°C
Minimum operating temperature	220	°C
Maximum operating temperature	450	°C
Specific heat, $c_{p,MS}$	1430	J/(kg•K)
Density, ρ	$-0.7264 \bullet T\ [°C] + 2240$	Kg/m^3
Thermal conductivity	0.52	W/(m•K)
Dynamic viscosity	$1.372 \bullet 10^9 \bullet (T\ [K]^{-3.364})$	mPa•s

the system.

The installation is directly connected to the local DHN supporting the decarbonization of the region, where an old coal-based combined heat and power (CHP) unit is under decommissioning. However, it should be noted that the investigated unit is a pilot system, the fit of the installation to the DHN low temperature (about 120 °C) requirements is not optimal due to the large temperature difference between the demand side and the minimum MS operating temperature. Full scale commercial installations are intended primarily for low to medium temperature (indicatively between 150 °C and 450 °C) industrial heat decarbonization. Additionally, the system has been proven for participation to the frequency regulation market, thanks to the fast response and activation time of the electric heater unit (as further discussed in Section 3.2.1), and it is used to further maximize the integral flexibility of the local grid and to increase revenue streams.

2.2. System operation

As described by the authors in [15], the system can operate under six different operating modes: charge (CH), discharge (DISCH), simultaneous charge and discharge (CH + DISCH), hot standby (IDLE HOT), cold standby (IDLE COLD) and hot/cold standby (IDLE H/C). The BMS provides the logic and control inputs to the different actuators to ensure smooth operation.

When starting the charging mode, the BMS selects the initial source and destination tanks. The source tank, from which the MS are sucked and pumped toward the EH, is the one at the highest level and lowest average temperature. The destination tank is the empty one (or the one at the lowest level). The MS pump is started, and the MS are initially circulated back to the same tank until the MS flow rate target conditions are met. Once the flow condition is met the EH is started at the set ramping rate. To have a gradual heating up of the system and ensure MS storage at maximum temperatures, MS flow is circulated to the destination tank only once the threshold of 350 °C is attained at the EH outlet. The charging operation continues until the source tank reaches

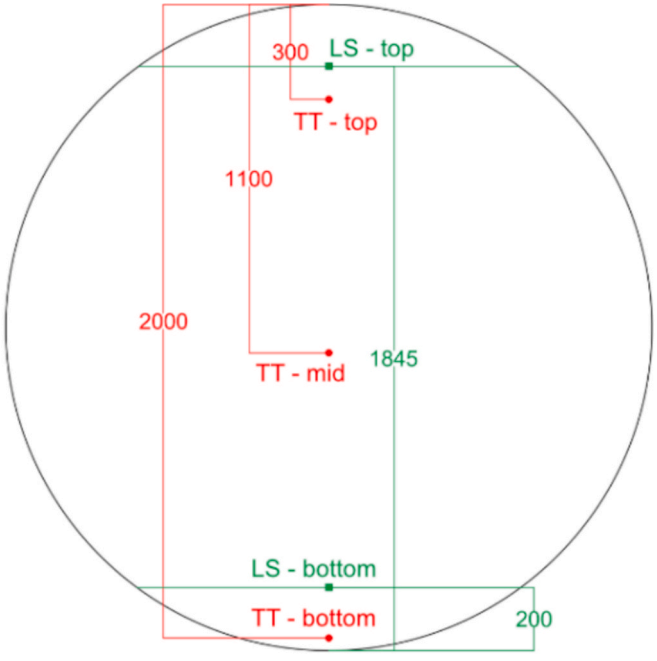

Fig. 3. Sketch of a section at mid length of a tank including annotations for the positioning of the main instrumentation (thermocouples, indicated by red dots, and top and bottom levels for the level sensor, indicated by green squares).

the minimum level (about 5 %). At this point the source tank is changed for the one at the highest level and lowest temperature among the remain ones and the previous source tank becomes the new destination tank. Once all tanks except one are filled with hot MS the charge procedure is complete and the system switch to hot standby. If the charge operation is terminated before all tanks are filled with hot salts, the IDLE H/C operation starts.

When starting the discharging mode, again the BMS selects the initial source and destination tanks. The source tank, from which the MS are sucked and pumped toward the SGS, is the one at the highest level and highest temperature. To guarantee a gradual heating up of the MS circulation pump (within a maximum temperature ramping rate of 60 °C/min) the pump starts circulating MS from the source tank through the SGS and part of it is bypassed and mixed with hot salts. Once the pump gradient is controlled and the unit is at hot condition all the MS is circulated from the source tank to the SGS and to the destination tank. Simultaneously, the DH water pump is started circulating cold water in the condenser and providing heat to the DHN. Once all tanks (except one) are filled with cold MS the discharge procedure is complete and the system switch to cold standby.

The main design points considered during the engineering of the described power-to-heat unit integrating TES are summarized in Table 2. The performance of the overall system is presented and analysed under both near design and off-design operation to provide a comprehensive assessment reflective of industrial installation. Table 3 summarizes the main parameters considered for the selection of the nearly-design and off-design operational cases.

2.3. Performance evaluation methodology

The system performance has been assessed comprehensively in nearly design, off-design operation and ramping up considering a set of key performance indicators (KPIs). The KPIs consider base operation focusing on energy efficiency and thermal losses, as well as EH ramping focusing on the EH thermal time constant and efficiency during transients. During operation the data are measured with a frequency up to 1 s and saved to the data logger system. To facilitate the data post-processing whilst guaranteeing accuracy, data have been extracted with a frequency of 10 s and post-processed accordingly.

2.3.1. Base operational performance

In steady state operation the system performance have been characterized primarily in terms of energy consumption and efficiency. Specifically, during charge, the total electric energy consumed by the EH has been evaluated as in Eq. (1), where $P_{EH,s}$ is the electric power measured by the meter in each of the four EH stages and $t_{end,ch}$ is the time at the end of the considered charge operation.

$$E_{EH} = \sum_{s=1}^{4} \int_0^{t_{end,ch}} P_{EH,s}(t)dt \tag{1}$$

The total thermal energy collected by the molten salts during the charging process by going through the EH has been calculated as in Eq. (2), where $\dot{m}_{MS}$ is the MS flow rate, $T_{EH,out}$ and $T_{EH,in}$ are the MS outlet and inlet temperature to the EH unit, and $c_{p,MS}$ is the MS specific heat, considered temperature independent and equal to 1.43 kJ/(kg•K) [29], respectively. It should be noted that limited MS specific heat variations with temperature have been highlighted in some previous preliminary characterization tests. However, no complete information is openly available at this time and the assumption of constant specific heat is considered sufficiently accurate within the context of the studied large scale system. More detailed salts characterization could enhance system control and responsiveness, but all considered KPIs would not be widely affected.

Table 2
Main design points of the investigated power-to-heat system.

Variable	Value	Unit
Electric power at EH	5	MW_e
Thermal power at SGS	4	MW_{th}
Thermal energy capacity	18	MWh

Table 3
Summary of the main operational parameters for the nearly design and off-design operations presented and discussed in section 3.1.1 (charge) and 3.1.2 (discharge). The values in parenthesis show the percentage with respect to the nominal values.

	Variable	Nearly design A – 18 Nov 2023	Off-design B – 7 Feb 2024	Unit
Charge	Average EH electric power, $\overline{P_{EH}}$	4.656 (93.1 %)	1.385 (27.7 %)	MW_e
	MS EH outlet temperature, $T_{EH,outMS}$	448 (99.6 %)	392.7 (87.3 %)	°C
Discharge	Average DH thermal power, $\overline{P_{DH}}$	2.869 (71.7 %)	1.884 (47.1 %)	MW_{th}
	MS SGS inlet temperature, $T_{SGS,inMS}$	416.2 (92.5 %)	358.6 (79.7 %)	°C
	H2O outlet temperature, $T_{SGS,outH2O}$	117.5 (97.9 %)	118.7 (98.9 %)	°C

$$E_{MS,ch} = \int_0^{t_{end,ch}} \dot{m}_{MS}(t)c_{p,MS}\left(T_{EH,out}(t) - T_{EH,in}(t)\right)dt \tag{2}$$

During discharge the total thermal energy provided to the DHN has been evaluated as in Eq. (3), where P_{DH} is the power measured by the meter at the DHN connection, at the end user side, and $t_{end,disch}$ is the time at the end of the considered discharge operation.

$$E_{DH} = \int_0^{t_{end,disch}} P_{DH}(t)dt \tag{3}$$

The total thermal energy delivered by the molten salts during the discharging process has been calculated as in Eq. (4), where $T_{SGS,outMS}$ and $T_{SGS,inMS}$ are the MS outlet and inlet temperature to the SGS unit, respectively.

$$E_{MS,disch} = \int_0^{t_{end,disch}} \dot{m}_{MS}c_{p,MS}(T_{SGS,inMS}(t) - T_{SGS,outMS}(t))dt \tag{4}$$

The MS level within each tank has been gathered directly from the level sensor. The reported MS temperature in each tank refer to the temperature reading at the mid-level thermocouple (at 1100 mm depth from the top of the tank). For tank 1, due to some thermocouple malfunctioning, the mean temperature between the top and bottom thermocouples is reported.

The duration of charge and discharge operation has been calculated as the time during which the EH and the condenser for DH are operating, also including their specific ramping up period but not including the additional time required for MS flow rate stabilization and pump temperature gradient control.

The efficiency of the system has been evaluated for both charge and discharge operation individually, as in Eqs. (5) and (6), respectively, as well as during the full process, round-trip efficiency, as in Eq. (7).

$$\eta_{ch} = \frac{E_{MS,ch}}{E_{EH}} \tag{5}$$

$$\eta_{disch} = \frac{E_{DH}}{E_{MS,disch}} \tag{6}$$

$$\eta = \eta_{ch} \cdot \eta_{disch} \tag{7}$$

The average temperature drops of the MS stored in the tanks during

standstill has been evaluated during both hot and cold standby, as in Eq. (8).

$$\frac{\Delta T_{TES}}{\Delta t} = \left[\frac{\sum_{i=1}^{N}(T_{TES}(i+1) - T_{TES}(i))}{N}\right] \cdot \frac{3600}{\Delta t} \quad (8)$$

where T_{TES} is the temperature measured at each of the three different thermocouples installed at different levels within the 6 tanks, N is the number of data samples for each considered standstill state and Δt is the sampling frequency of 10 s. Considering the range of MS storage temperature attained during different operations of the unit, hot standby is assumed with MS temperature in the range 360 °C–450 °C and cold standby for MS temperature in the range 180 °C–280 °C.

2.3.2. Start up and ramping performance

The ramping and start up performance represent a critical indicator for the system as faster response time, particularly for the EH, can maximize the system's flexibility as well as potential revenue streams from participation in the frequency regulation market.

To assess the response time of the charging loop in the presence of a request from the grid operator for downward frequency regulation, the time required for the EH to draw the design 5 MW_e from the grid starting from a cold standby operation has been recorded via a set of start-up tests done, also in collaboration with the local electricity grid operator (ENERGINET [31]). This time span includes also the required initial BMS activation, valves opening, and MS flow stabilization prior to starting the EH, as well as the EH ramping from 0 MW_e to 5 MW_e.

The specific performance of the EH under ramping has been further investigated by assessing its thermal time constant and efficiency during 30 different ramping operations. These performance indicators are widely required for dynamic modelling and control applications and are here reported over a broad range of testing operation, also indicating their dependence against key operating conditions as MS flow rate and initial temperature. The thermal time constant, τ, is widely used to describe the response of a thermal system, such as heat exchangers [32,33], to a step input and it represents the time elapsed from start until the system's response reaches $(1-e^{-1}) \approx 63.2\%$ of its steady state value. Specifically, in this work the thermal time constant, τ, of the EH has been evaluated considering a step increase of the EH power, P_{EH}, and the MS outlet temperature, $T_{EH,out}$, is considered as the main system's response. The EH thermal time constant, τ, has been calculated from Eq. (9).

$$\frac{T_{EH,out}(t) - T^{0}_{EH,out}}{T^{\infty}_{EH,out} - T^{0}_{EH,out}} = 1 - \exp\left\{-\frac{(t-\delta)}{\tau}\right\} \quad (9)$$

where $T^{0}_{EH,out}$ is the MS outlet temperature at the initial time, $T^{\infty}_{EH,out}$ is the MS outlet temperature once steady state conditions are attained, and δ is the unit's delay, which is physically equivalent to the residence time of the MS in the EH. The specific working conditions, MS average flow rate and temperature at τ, in each test have been accounted for in the evaluation of δ, which has been calculated as from Eq. (10).

$$\delta = \delta_{ref}\left(\frac{\dot{m}_{ref}}{\dot{m}}\right)\left(\frac{\rho}{\rho_{ref}}\right) \quad (10)$$

where $\dot{m}_{ref}$ is the design MS mass flow rate equal to 15 kg/s, ρ_{ref} is the MS density at the design temperature of 400 °C, and δ_{ref} is the reference delay at design working conditions equal to 120 s. The MS density has been considered temperature dependent as from the data shown in Table 1.

It should be highlighted that considering the size of the equipment (5 MW_e) an instantaneous step change of the EH power is not physically attainable. However, power ramping values in the range 10–50 kW/s have been considered. They are sufficiently high to ensure relevant consistency of the analytical temperature provided by Eq. (9) and the recorded data, which lays in within a ±10 % range of the analytical curve, as shown in the Appendix. It should be noted also that for all 30 considered operations the MS inlet t

emperature to the EH is kept constant (with a maximum variation within 1 % of its average). Therefore, evaluating the thermal time constant on the MS temperature difference across the EH would lead to the same outcomes.

The EH efficiency during the unit's ramping up and its dynamic response has been evaluated during different time spans in the range between 1 and 8-times thermal time constants intervals. Specifically, two main time intervals have been highlighted: (1) the initial ramping before reaching the unit's thermal time constant, at $t \leqslant \tau$, which is representative of the initial fast response of the system; and (2) the initial period equivalent to four thermal time constants, at $t \leqslant 4\tau$, which is shown in literature [34] to lead to about 98 % of the steady state target, comparable with the end of the initial transient and the completion of the EH ramping up process. The EH efficiency calculated during the first period, at $t \leqslant \tau$, is expected to record low values as majorly affected by the system thermal inertia. The dynamic efficiencies calculated during the initial ramping process (and at different time intervals between 1 and 8-time the thermal time constant) have been differentiated from the unit efficiency. Specifically, the EH ramping up efficiencies have been evaluated as in Eq. (5), but the integrals in Eqs. (1) and (2) have been applied for $t \in [0, \tau]$, for the initial ramping up efficiency before reaching the unit's thermal time constant, $\eta^{\tau}_{ramp-up}$. Similarly, for all other EH ramping up efficiencies calculated at different multiples of the unit's thermal time constant, $\eta^{x\tau}_{ramp-up}$, the integrals in Eqs. (1) and (2) have been applied for $t \in [0, x{\cdot}\tau]$, where x is multiple of the unit's thermal time constant (in the range between 1 and 8).

3. Results and discussion

The following sections present and discuss the main outcomes considering design operation in charge, discharge as well as simultaneous operation. The overall operation is presented for a few relevant days representative of the main behaviour of the system under nearly design (within a margin of less than −30 %) (A-18 Nov 2023), and at off design operation (B-7 Feb 2024), as listed in Table 3. The typical system operation is shown also during simultaneous charge and discharge operation (as measured on 14 December 2023).

The choice of the selected representative days started from the actual operating data of the unit, and it considers average power consumption and delivery, average operating temperatures and duration of the cycles aiming at presenting a comprehensive overview of the unit's performance under relevant working conditions. It should be highlighted that the system is expected to operate primarily in design and close to design operating conditions, particularly during the charging process to maximize the use of cheap and renewable available power. Thus, the design operating performance should be considered as the most relevant ones and the target for further performance optimization. The last section presents the dynamic response of the electric heater and its efficiency during ramping up periods.

3.1. Base operation

3.1.1. Charge operation

Fig. 4 summarizes the main operating performance of the studied system during a typical charging cycle at nearly design operation (A – 18 Nov 2023). Fig. 5 presents the main operating performance of the studied system during a typical charging cycle at off-design conditions (B – 7 Feb 2024). The top charts report the MS temperatures at the inlet and outlet of the EH, the MS mass flow rate and the electric power consumed by the EH. The middle charts show the temperature of the MS contained in each of the tanks as measured at the mid thermocouple

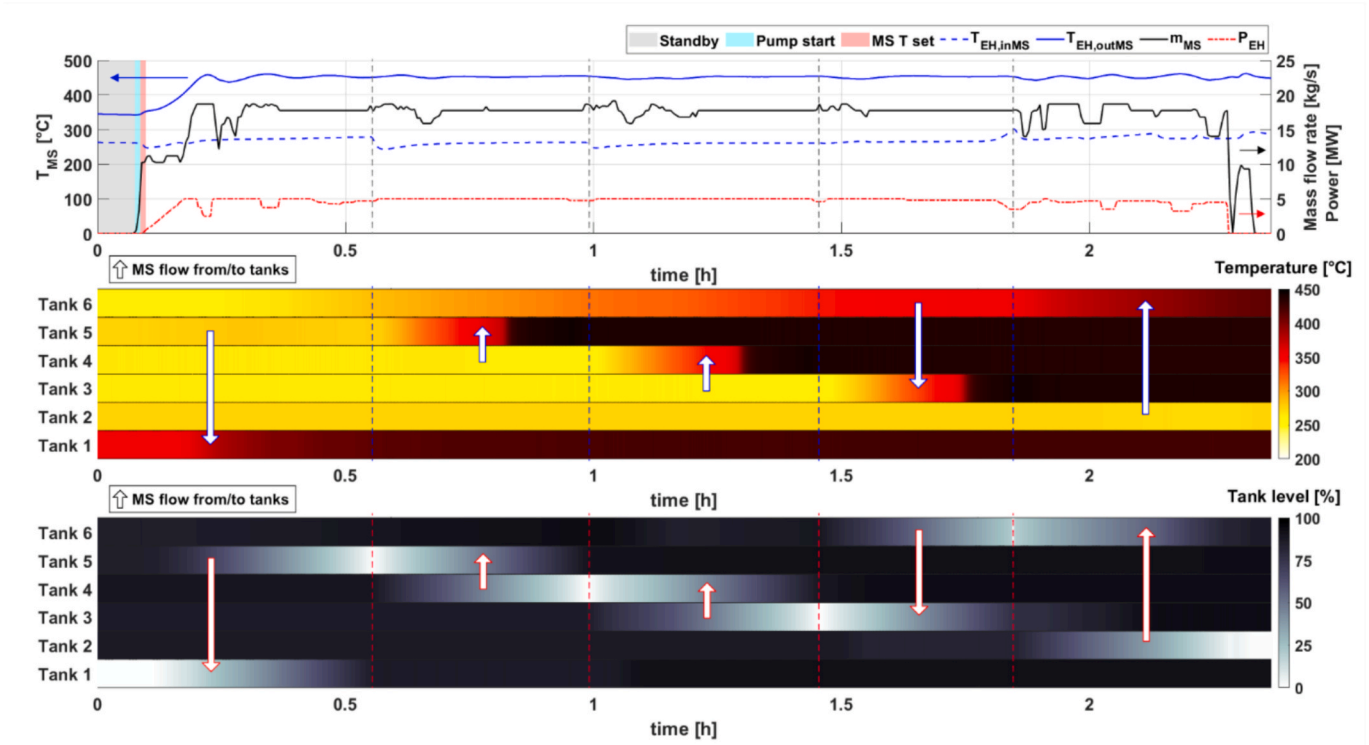

Fig. 4. Overview of the system's performance during a typical charge cycle at nearly design operating conditions (A-18 Nov 2023): (top) MS temperatures at inlet and outlet of the EH, MS mass flow rate and EH electric power; (middle) MS temperatures at the mid-level thermocouple for the 6 tanks also including MS flow direction in between tanks during operation; (bottom) MS level within the 6 tanks also including MS flow direction in between tanks during operation.

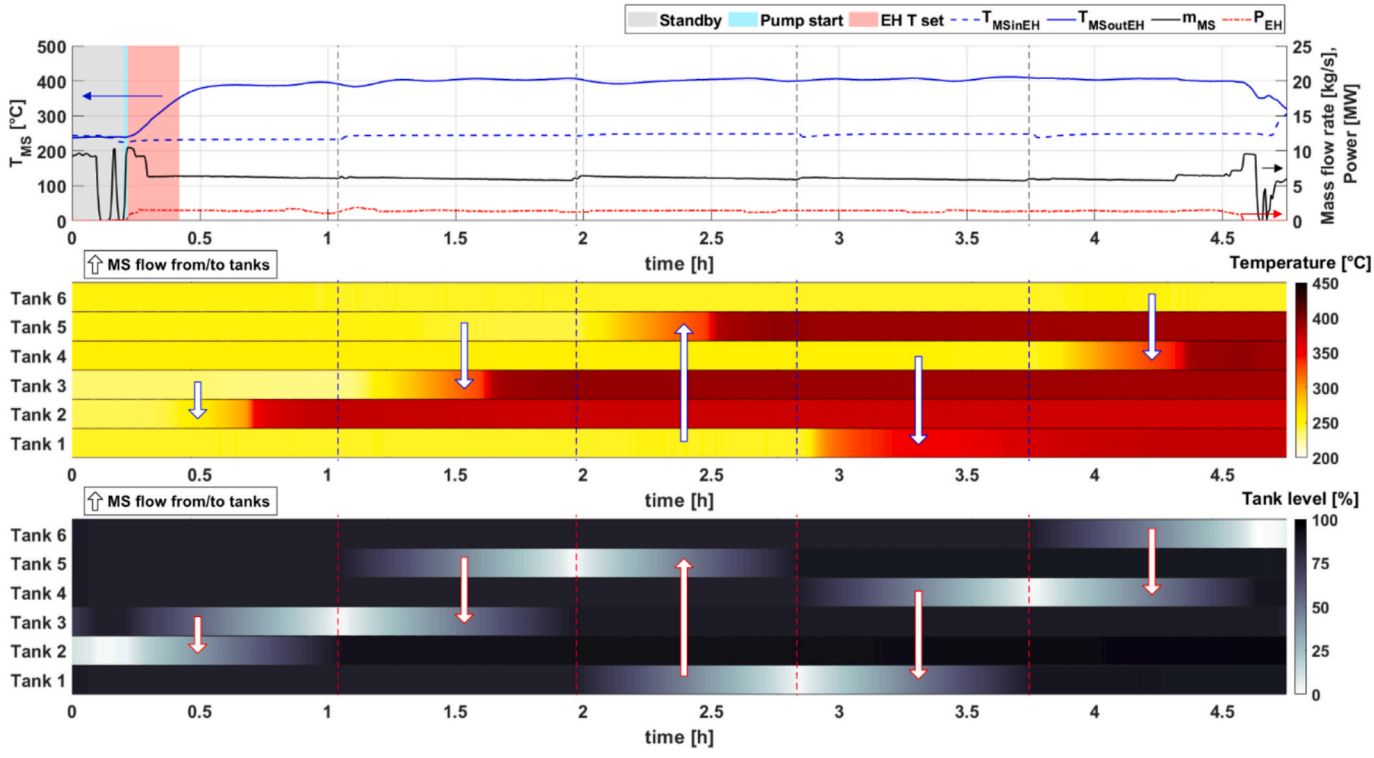

Fig. 5. Overview of the system's performance during a charge cycle at off-design operating conditions (B – 7 Feb 2024): (top) MS temperatures at inlet and outlet of the EH, MS mass flow rate and EH electric power; (middle) MS temperatures at the mid-level thermocouple for the 6 tanks also including MS flow direction in between tanks during operation; (bottom) MS level within the 6 tanks also including MS flow direction in between tanks during operation.

(1100 mm depth) during the full operation. The bottom charts report the MS level in the six tanks, arrows are used to indicate the MS flow direction from and to the tanks and the dashed lines indicate the moment when tanks are switched. Table 4 summarizes the main KPIs as calculated for both cases.

In the initial stages of the charging process, in both considered operational cases, once the standby is terminated, the BMS is started to select the operating tanks and the actuators are activated for valves positioning. Then, the MS pump is started and reaches stable flow conditions in a short time interval (in the range 40–60 s, light blue area in Figs. 4 and 5). The required MS recirculation to the source tank in the initial phase of the charge operation largely depends on the initial MS temperature, since an EH outlet temperature of 350 °C needs to be attained before MS is delivered to the destination tank. On day A at a high initial MS temperature of 343.5 °C, the MS recirculation only lasts for 40 s (red area in Fig. 4). On day B at a lower initial MS temperature of 238.7 °C, it requires about 730 s (red area in Fig. 5).

After the initial ramping of the EH, which is further discussed in Section 3.2, the system operates under stable conditions. Elevated stability and controllability of the system can be highlighted particularly when considering the system under design operating conditions (day A). Specifically, in nearly design operation, variations of the electric power at the EH can be effectively compensated for by an adjustment of the MS mass flow rate still guaranteeing average MS outlet temperatures of about 448 °C and a standard deviation of the temperature limited to 3.83 % (equivalent to about 17 °C). Similarly, the MS inlet temperature to the EH unit is almost constant during the full charging operations with maximum standard deviations of <10 °C (equivalent to <3.5 %). It can be also noted that the implemented control system considers a temperature independent MS specific heat. The recorded performance and their stability further validate the sufficient accuracy of this simplification. However, it should be highlighted that further detailed knowledge about MS properties evolution with temperature and time, once implemented within the control logic, would likely lead to further performance improvements, particularly when considering responsiveness of the unit, and enhanced stability. Wider changes of the MS inlet temperature are recorded around the switchovers between source and destination tanks (close to the dashed vertical lines). The MS inlet temperature drops by about 26 °C at the switchover point, when the MS is pumped from a new source tank. This is caused by the fact that the MS must flow via different pipes and valves which would present lower temperatures and thus their initial thermal inertia must be overcome, and a limited loss occurs by heating up the newly activated sections of pipeline.

The level data effectively report how the tanks are managed and clarify the operation and switchover between source and destination tanks. Specifically, in the considered days, at the beginning of the charge operation the full system is at a cold standby status with five tanks filled with cold salt and an empty tank (tank 1 in day A and tank 2 in day B). On day A, in nearly design operation, the charge process ends at an almost fully charged system with tank 1, 3, 4, and 5 up to about 445 °C, and tank 6 filled with salts up to an average 400 °C, whilst tank 2 is empty. The temperature charts show a smooth initial temperature increase when a new tank is selected as the destination one, followed by a relatively sharp temperature increase between 350 °C and 440 °C, and a stable temperature at the maximum level during the second part of the single tank process. This trend is justified by the fact that the considered thermocouple is installed at an intermediate depth (1100 mm, equivalent to about 50 % of the total volume). Thus, once the MS reaches the thermocouple level, the thermocouple will only see minor temperature changes due to MS mixing. Similar behaviours can be observed under off-design operation. The order of exploitation of the tanks is different from the one in day A, and the coldest tank among the full ones (tank 3) is first activated as the initial source tank. This operation follows the criteria set in the BMS, and explained in Section 2.2, based on which during charge the first source tank is the one at the lowest temperature and highest level. The flexible approach enables to maximize the effectiveness of the charging pattern and maximizing the TES overall temperature and energy content. In day B in off-design operation, at the end of the charge process five tanks are filled with hot MS, however the temperature is limited to about 388 °C. Due to the lower EH load and longer temperature ramping (with respect to day A), tank 2, the first destination tank, remains filled with lower temperature salts at about 369 °C. The charge process presents elevated efficiency, after initial transients, even at partial load operation. Average charging thermal efficiency of about 97.3 % is measured under nearly design operation (at an average EH load of 4.656 MW equivalent to 93.1 % of the nominal 5 MW_e). Limited reductions are measured, with charging thermal efficiency down to 95.7 %, at operation in partial load (at an average EH load of 1.385 MW equivalent to 27.7 % of the nominal 5 MW_e). It can be also observed that in order to maintain elevated thermal efficiency keeping the working temperatures closer to the design point is beneficial. Thus, in the off-design case (day B) the control acts primarily upon the MS flow rate with an average reduction of about 65 %, whilst the temperature increment within the EH is only reduced by about 18 %. Similar control suggestions could be applicable to comparable technological solutions. Overall, it can be observed that off-design operations, with temperatures farther from the design points, negatively affects the system performance more than other possible off-design working conditions. Therefore, it can be suggested that off-design operations and relative dynamic control systems should prioritize operation in partial load via control on the MS mass flow rate aiming at reduced impact on the MS temperature.

Table 4
Summary of the KPIs for a charging cycle during the two considered reference days.

Parameter	Nearly design A – 18 Nov 2023	Off-design B – 7 Feb 2024	Unit
Charge duration, $t_{end,ch}$	7900 (131.6)	15,930 (265.5)	s (min)
Average EH power, $\overline{P_{EH}}$	4.656	1.385	MW_e
Charged energy, E_{EH}	10.22	6.13	MWh_{th}
Average MS EH outlet temperature	448.0	392.7	°C
Standard deviation of $T_{EH,outMS}$	17.15 (3.83 %)	30.96 (7.88 %)	°C
Average MS EH inlet temperature	266.1	243.4	°C
Standard deviation of $T_{EH,inMS}$	9.44 (3.55 %)	6.52 (2.68 %)	°C
Charge efficiency, η_{ch}	97.3	95.7	%

3.1.2. Discharge operation

Fig. 6 summarizes the main operating performance of the studied system during a typical discharging cycle at close to design load (A – 18 Nov 2023). Fig. 7 presents the main operating performance of the studied system during a discharging cycle at partial load (B – 7 Feb 2024). The top charts report the MS and water temperatures at the inlet and outlet of the SGS, the water temperature as delivered to the DH grid, the MS and water mass flow rate and the thermal power provided to the DHN. The middle charts show the temperature of the MS contained in each of the tanks as measured at the mid thermocouple (1100 mm depth) during the full operation. The bottom charts report the MS level in the six tanks, arrows are used to indicate the MS flow direction from and to the tanks and the dashed lines indicate the moment when tanks are switched. Table 5 summarizes the main KPIs as calculated for both cases.

Once the signal to start the discharge procedure is sent to the BMS, the hot standby operation (grey area in Figs. 6 and 7) is terminated, the valves are set in the required positions, and the MS pump is started. With respect to the operation under charge, in discharge the MS pump needs to circulate hot (above 400 °C) molten salts, thus a more rigid warming up procedure is required in which a maximum heating rate of 60 °C/min is fixed for the pump structure and partial salt flow bypass is exploited.

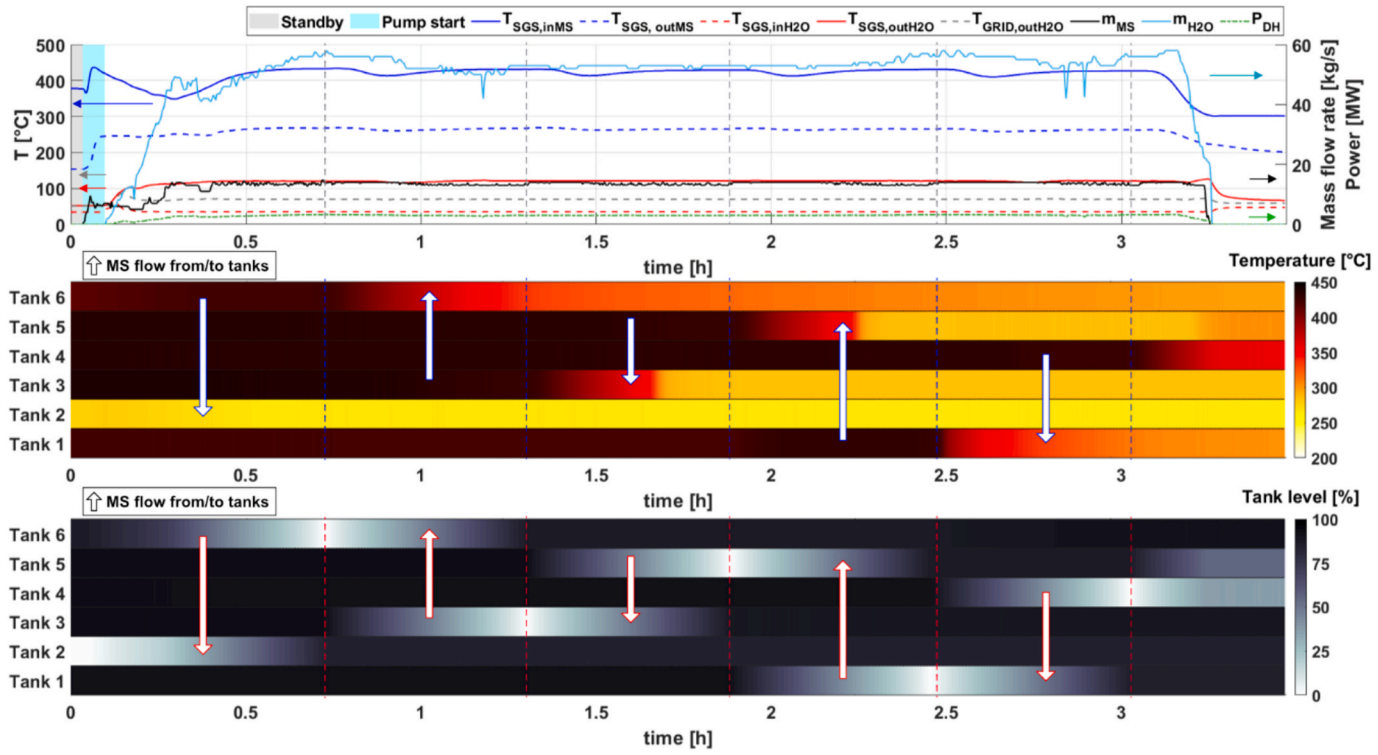

Fig. 6. Overview of the system's performance during a typical discharge cycle at nearly design load (A-18 Nov 2023): (top) MS and water temperatures at inlet and outlet of the SGS, water temperature at DHN delivery point, MS and water mass flow rate and DH thermal power; (middle) MS temperatures at the mid-level thermocouple for the 6 tanks also including MS flow direction in between tanks during operation; (bottom) MS level within the 6 tanks also including MS flow direction in between tanks during operation.

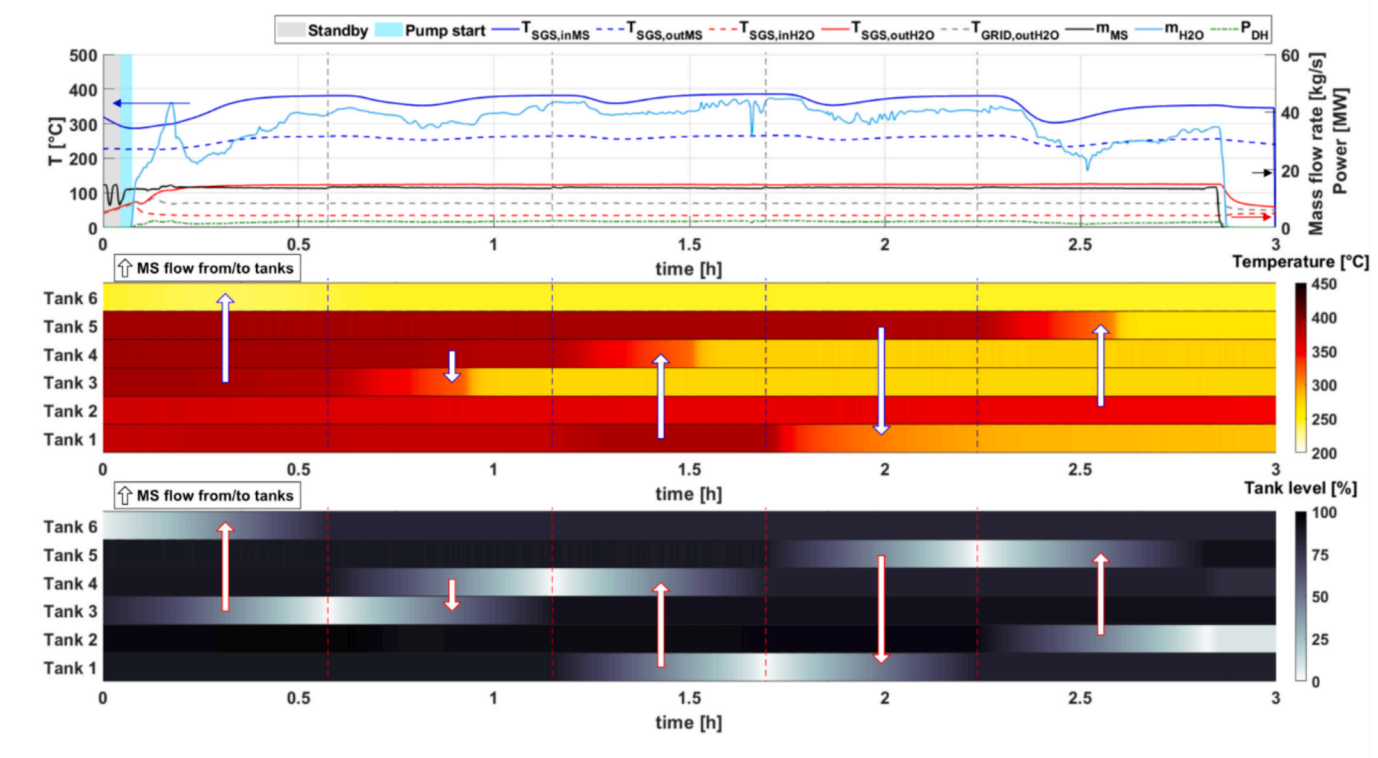

Fig. 7. Overview of the system's performance during a discharge cycle at off-design conditions (B – 7 Feb 2024): (top) MS and water temperatures at inlet and outlet of the SGS, water temperature at DHN delivery point, MS and water mass flow rate and DH thermal power; (middle) MS temperatures at the mid-level thermocouple for the 6 tanks also including MS flow direction in between tanks during operation; (bottom) MS level within the 6 tanks also including MS flow direction in between tanks during operation.

Table 5
Summary of the KPIs for a discharging cycle during the two considered reference days.

Parameter	Nearly design A – 18 Nov 2023	Off-design B – 7 Feb 2024	Unit
Duration discharge, $t_{end,disch}$	11,380 (189.7)	10,490 (174.8)	s (min)
Average DH power, $\overline{P_{DH}}$	2.869	1.884	MW
Discharged energy, E_{DH}	9.07	5.49	MWh
Average MS SGS inlet temperature	416.2	358.6	°C
Standard deviation of $T_{SGS,inMS}$	23.53 (5.65 %)	26.07 (7.27 %)	°C
Average MS SGS outlet temperature	260.3	254.5	°C
Standard deviation of $T_{SGS,outMS}$	12.22 (4.69 %)	11.06 (4.35 %)	°C
Average water SGS inlet temperature	35.3	35.9	°C
Standard deviation of $T_{SGS,inH2O}$	1.95 (5.52 %)	3.96 (11.03 %)	°C
Average water SGS outlet temperature	117.5	118.7	°C
Standard deviation of $T_{SGS,outH2O}$	11.64 (9.91 %)	15.95 (13.44 %)	°C
Discharge efficiency, η_{disch}	97.45	94.0	%
Round trip efficiency, η	94.60	89.96	%

This procedure causes and ramping up periods between 100 s and 250 s longer than the ones registered during the charge phase. Once the MS pump temperature and relative MS flow rate minimum set points are reached the water pump for the water flow through the SGS is started. In the selected cases, the water flow and consequent thermal power delivery to the DHN is ramped up to the target power in about 5–15 min. Depending on the specific operating conditions, from the moment the input signal to start discharge is sent until reaching set working conditions and target thermal power delivery to the DHN, the installed unit requires between 15 and 25 min. This timing should be properly considered for operation planning to allocate the required timespan for pre-heating whilst ensuring a proper fulfilment of the demand and limiting negative impacts on the system's flexibility.

Once the target operating conditions are attained, the installation operates quite constantly and uniformly. The MS inlet temperature to the SGS is maintained at about 416 °C, under close to design operating conditions, and 359 °C, in off-design discharge process. Thermal losses, as further discussed in Section 3.1.4, contribute in a reduction of the MS SGS inlet temperature of about 30–35 °C when compared to the EH MS outlet temperature attained during the previous charge process. A MS SGS inlet temperature drop between 15–25 °C is noticeable, shortly after each switchover of the source tank. As for the charge operation, this temperature drop is primarily caused by the fact that when changing to a new source tank, a different section of the circulation loop must be activated and warmed up by the flowing salts.

Figs. 6 and 7 show the tanks operation and switchover. It can be noted that no prefixed discharge tanks activation sequence is set, rather the most suited source and destination tanks are selected based on specific level and average MS temperature. This feature not only improves the system's flexibility and adaptability to users' needs but it also ensures resilience and facilitates maintenance procedure reducing downtimes.

The discharge process is characterized by elevated thermal efficiencies of about 97.5 % at nearly design point and down to about 94 % at off-design operation. This leads to an overall thermal round trip efficiency of the installation higher that 94 % under design operation and of about 90 % at partial load operation. From a control perspective, to guarantee elevated performance, it is suggested to maintain the MS loop operating conditions close to the design point and adjust primarily the water loop operating points (at first the mass flow rate) to control the delivered power.

3.1.3. Simultaneous charge and discharge operation

Fig. 8 summarizes the main operating performance of the studied system during a simultaneous charge and discharge operation and it highlights two specific operating phases. In phase 1 (highlighted by a yellow background), the EH operates at the design load of 5 MW_e, a sensibly higher average power than the thermal power delivered to the DHN of about 3.4 MW_{th}. Thus, it enables a slow rate charging of the TES unit. In phase 2 (highlighted by a green background), the power produced by the EH is directly transmitted to the DHN via the MS loop. In this phase the system is basically operated as an electric boiler at lower efficiency. However, the system's ability to operate under this condition provides essential flexibility to the full unit. Indeed, charge and discharge operation can be fully decoupled enabling to charge the unit whenever it is more convenient whilst making sure to fulfil the user requirements.

In Fig. 8 the top charts report the MS temperatures at the inlet and outlet of the EH and of the SGS, the MS mass flow rate flowing through the EH and the SGS and the power consumed by the EH and provided to the DHN. The middle charts show the temperature of the MS contained in each of the tanks as measured at the mid thermocouple (1100 mm depth) during the full operation. The bottom charts report the MS level in the six tanks, arrows are used to indicate the MS flow direction from and to the tanks and the dashed lines indicate the moment when tanks are switched. Table 6 summarizes the main KPIs as calculated for the two phases, average values are reported over the highlighted timespan in the top chart.

The simultaneous operation presents ramping procedures similar to the ones highlighted for the single operations of charge and discharge. During operation in both phases, stable temperatures can be highlighted with standard deviations limited below 2 °C, equivalent to less than 1 % standard deviation. During both phase a limited temperature increment, below 0.3 °C, between the average MS EH outlet temperature and the average MS SGS inlet temperature can be observed. This can be explained by both the activation of local heat tracing and residual heat in the system, as well as by the error margin of the thermocouples. During phase 1, the TES charging occurs at a lower rate with an effective power available for TES charging of about 1.6 MW (equivalent to about 32.4 % of the EH design load), which is also visible via the slower rate of average MS temperature and level increase in tank 3. During phase 2, the TES units are not used as visible by the constant MS level. As mentioned before, phase 2 behaves like a direct boiler with lower efficiency due to the intermediate MS loop. However, since, in the considered case, no thermal inertia need to be overcome, the round trip efficiency is still above 98 %. Thus, considering that such operating mode is foreseen only during limited timespan (as highlighted by the authors in [15]), the limited losses are compensated by the increased system flexibility advantageous to ensure full reliability and on-demand industrial heat generation.

3.1.4. Thermal losses in standstill

Thermal losses from the TES unit are a key parameter for the development of intraday and long duration TES units. Fig. 9 shows the measured temperature drop in the different tanks during the two main cases discussed in Sections 3.1.1 And 3.1.2. As expected, the temperature drop is dependent on the average MS temperature within the TES unit. Thus, the data are divided and reported for both hot (360–440 °C) and cold (200–280 °C) conditions. Average results for typical cold stage and hot stage, as well as the data linear fitting against the MS average temperature, are also shown. Table 7 summarizes the average, μ, and median, *Md*, values and the linear fitting. A linear fitting has been adopted as it provides the most accurate fitting among other first order methods. Additionally, considering the limited height of the TES tanks, the thermal losses are expected to be dominated by thermal conduction through the TES wall and insulation layers.

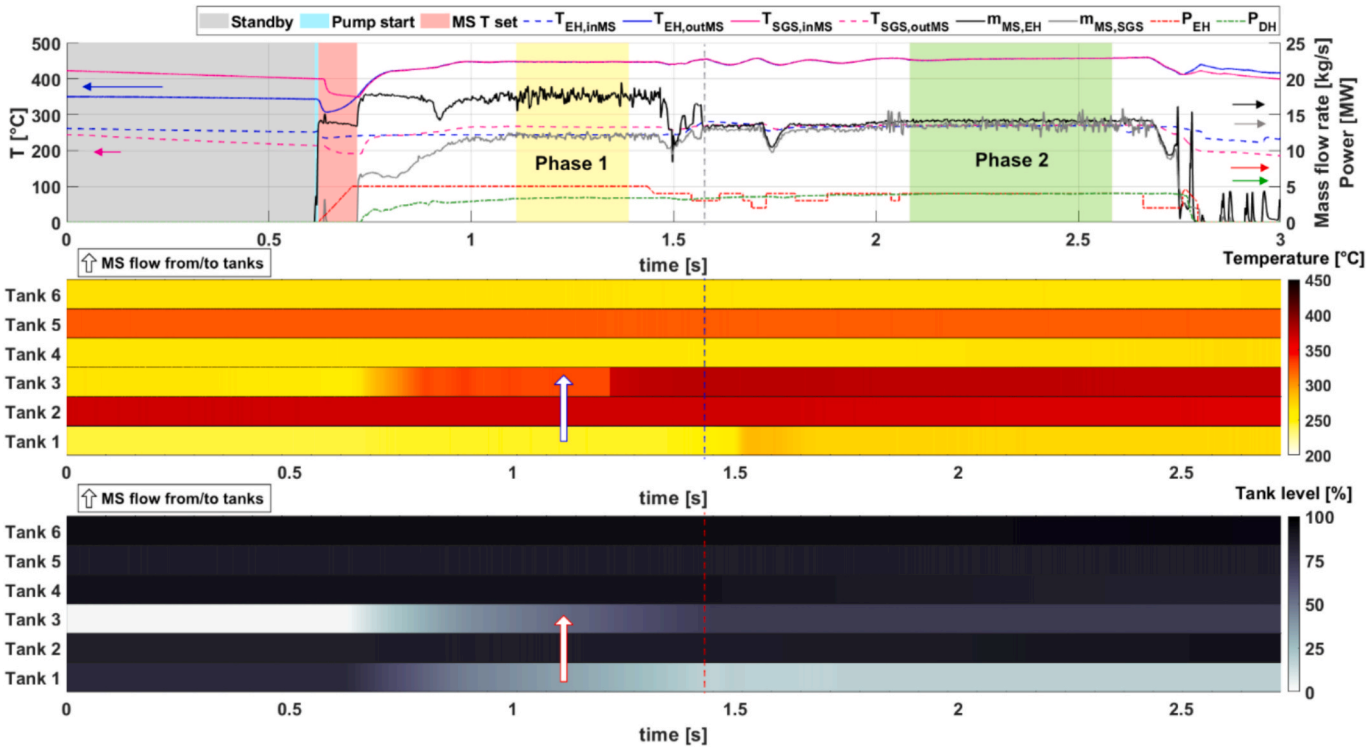

Fig. 8. Overview of the system's performance during a simultaneous operation: (top) MS temperatures at inlet and outlet of the EH and SGS, MS mass flow rate through the EH and SGS, EH power and DH thermal power; (middle) MS temperatures at the mid-level thermocouple for the 6 tanks also including MS flow direction in between tanks during operation; (bottom) MS level within the 6 tanks also including MS flow direction in between tanks during operation.

Table 6
Summary of the KPIs for a reference simultaneous operation of the system.

Parameter	Phase 1	Phase 2	Unit
Average EH power, $\overline{P_{EH}}$	5.014	4.015	MW_e
Average DH power, $\overline{P_{DH}}$	3.384	3.973	MW_{th}
Average MS EH outlet temperature	446.9	455.0	°C
Standard deviation of $T_{EH,outMS}$	0.39 (0.09 %)	1.87 (0.41 %)	°C
Average MS EH inlet temperature	243.9	268.4	°C
Standard deviation of $T_{EH,inMS}$	0.03 (0.01 %)	0.63 (0.23 %)	°C
Average MS SGS inlet temperature	447.2	455.2	°C
Standard deviation of $T_{SGS,inMS}$	0.37 (0.08 %)	1.82 (0.40 %)	°C
Average MS SGS outlet temperature	265.7	270.4	°C
Standard deviation of $T_{SGS,outMS}$	0.92 (0.35 %)	0.26 (0.09 %)	°C

During cold standby (with salts kept in the temperature range 200–280 °C), an average temperature drop of −0.56 °C/h is recorded. However, most data points present value above −0.5 °C/h, and two outliers can be noted at about −1.2 °C/h and −3.6 °C/h, resulting in a median value of −0.46 °C/h. The outliers are due to tanks 3 and 5 and are likely caused by specific thermal bridges and poorer insulation. During hot standby (with MS in the range 360–440 °C), a wider spread of the data points is visible, and an average temperature drop of −2.33 °C/h is recorded. The measured thermal losses are considered satisfactory as in line with literature data presented for binary salts applications. Specifically, when compared they are higher than for large scale CSP MS tanks, which report losses around 0.5 °C/h limited by the large size of the TES tanks (diameters above 30 m and 15 m height) and thicker insulations [35]. The recorded thermal losses are comparable to modelled CSP TES tank losses with comparable insulation thickness [35], and lower than smaller scale installations reporting temperature drop up to 4.5 °C/h [36].

When considering the typical operation cycle of the investigated power-to-heat system for industrial heat decarbonization, typical standby periods between 2 and 12 h are foreseeable. In particular a

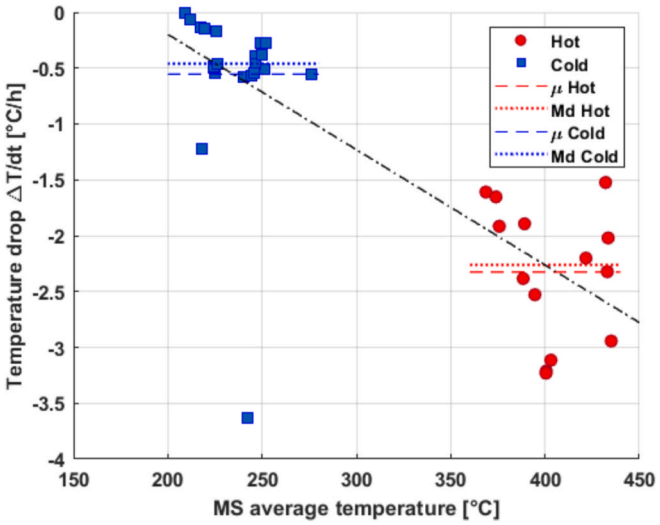

Fig. 9. Average temperature drops in the different TES tanks at different MS average temperatures during standstill. Data points shown from different operative days, average values and linear fitting showed by the dashed and dotted lines for typical cold and hot MS conditions.

previous work from the author showed that overall the system is expected to be on stand-by operation for about 25 % of the lifetime, and primarily in cold standby (IDLE COLD) (about 20 % of the lifetime), and only 1 % in hot standby (IDLE HOT) [15]. Considering the reported data and a maximum standby period of 12 h at cold and hot conditions, a total temperature drop of about 6 °C and 30 °C, respectively, can be estimated. The results show that for similar modular power-to-heat systems integrating MS based TES, longer standby periods than intraday (more than 12 h) are not suggested as they would result in

Table 7
Overview of the average temperature drop from the TES and specific ranges of validity for the MS temperature.

Parameter	Value (range)	Unit
Average temperature drop in hot standby	−2.33 (360–440 °C)	°C/h
Median temperature drop in hot standby	−2.26 (360–440 °C)	°C/h
Average temperature drop in cold standby	−0.56 (200–280 °C)	°C/h
Median temperature drop in cold standby	−0.46 (200–280 °C)	°C/h
Linear fitting of temperature drop	$-0.0103 \cdot \bar{T}_{MS} + 1.8665$	°C/h

detrimental energy losses. Improvements in the insulation material performance or thicker insulation layers can limit the losses at the expenses of additional capital costs. The results also highlight that thermal losses should be accurately modelled when considering the system operational performance and dispatch strategies since different charging patterns might be preferred to ensure lowered energy losses throughout the full operational cycle.

3.2. Electric heater dynamic response

The sections below describe and discuss the main results obtained for the dynamic and start up response of the EH unit, which represents the most critical components for the studied flexible power-to-heat system integration and connection with the electrical grid. An EH with fast responses and ramping can enable the unit to participate in downward frequency regulation, maximize the potential for resiliency services to the grid as well as associated revenues opportunities.

3.2.1. Frequency restoration reserve response test

Fig. 10 shows the main performance of the EH unit during one of the frequency restoration reserve (FRR) market tests, and it highlights the main operational phases. Table 8 summarises the main timing required by each operational step and the main operating conditions.

The initial operational phase, 'Standby + BMS', shows the time required from the moment the procedure is started and the main signal to start charge is sent to the BMS to the moment the MS pump is started. In this time, the BMS identify the suited tanks to operate as source and destination, acts on the circulation loop to open and close the different valves depending on the selected tanks and finally send the activation signal to the pump. This is the most impactful time interval lasting about 50 s, which highlights that simplified circulation loops and control systems could largely benefit not only the construction time and costs but also the responsiveness and flexibility of MS based power-to-heat

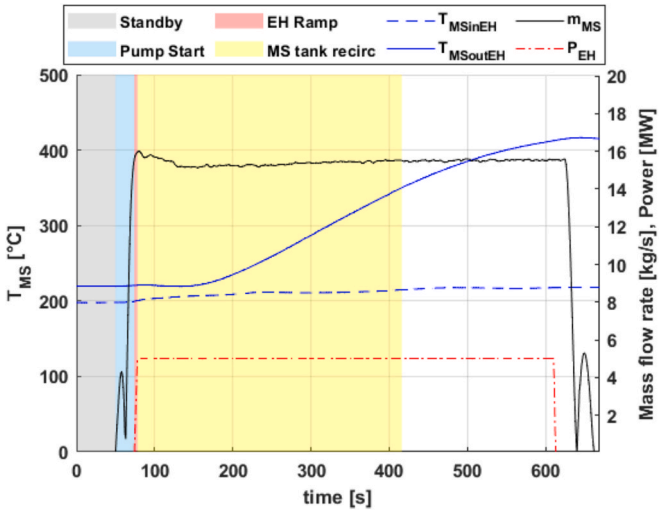

Fig. 10. Overview of the main EH performance during one of the frequency market regulation tests (EH start up procedure).

Table 8
Summary of main performance during EH response test.

Parameter	Value	Unit
Time in cold standby for BMS starting	50	s
Time for pump ramping up and MS flow stabilization	24	s
Time for EH electric power ramping	4	s
Time to reach MS set temperature (350 °C) at EH outlet	338	s
Average MS flow rate	15.43	kg/s
Average EH electric power	5	MW_e

units and the consequent possibility to operate in various electricity markets. Once the stating signal is received by the cold MS pump, it follows a similar ramping up ('Pump start') as highlighted for the charge operation, which requires about 24 s. The EH electric ramping up ('EH Ramp') is the fastest phase and takes place in only 4 s. This represents the time required for the electric power consumption at the EH grid connection to raise from 0 to 5 MW_e.

Thus, summing up all the main phases, the investigated system requires about 78 s from the moment the 'start charge' signal is sent from the grid operator to the moment it can effectively withdraw 5 MW_e from the electric grid. The results highlight the compatibility of the investigated system to comply with standard activation time requirements for automatic frequency restoration reserve of 5 min [37]. The result also proves the suitability of MS power to heat systems to provide local grid stabilization services and specifically to take part in up and downward frequency regulation services. The investigated system could be considered within the pool of technologies able to support frequency restoration alongside electrochemical batteries, pumped hydro and gas turbines [38].

3.2.2. Thermal time constant

As described previously, the thermal time constant for the EH represents the response of the unit to a step input and specifically the time elapsed from start of a step change in the EH electric power until the MS outlet temperature reaches $\left(1-e^{-1}\right) \approx 63.2\%$ of its steady state value. Thus, shorter time constant can ensure faster system response and increased system flexibility. In this study, the EH thermal time constant has been evaluated considering 30 different real operational cases with variable MS initial temperature, MS inlet temperature, MS steady state target temperature, EH power and MS mass flow rate. Fig. 11 summarizes the main distribution of the calculated thermal time constants. It can be noted that the most common range of the thermal time constant is

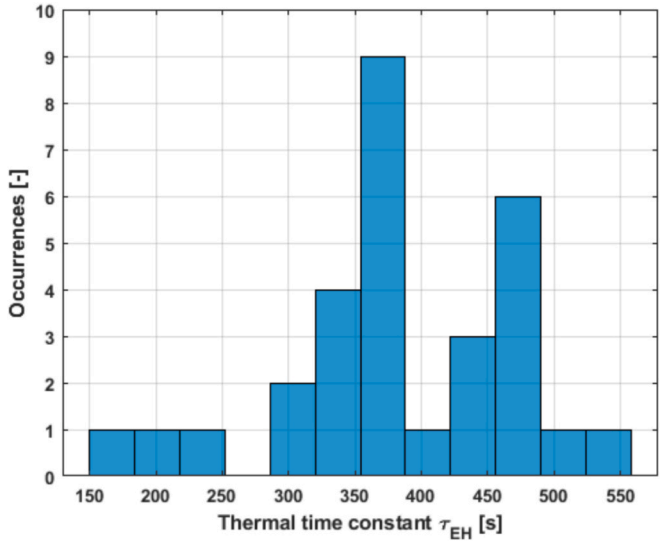

Fig. 11. Histogram showing the occurrences of different thermal time constants.

between 320 s and 388 s with 13 total occurrences (43 %), followed by the range 422 s–490 s with 9 occurrences (30 %). When compared to the design residence time of the EH of about 120 s, the limited thermal time constants of the unit reflect an effective heat transfer attained by the EH unit. This result also confirms the suitability of similar EH designs for flexible operation and rapid thermal response.

Fig. 12 summarizes the correlation coefficients between different operating conditions of the EH and the main dynamic KPIs (Fig. 12 (a)), as well as among the dynamic KPIs (Fig. 12 (b)). The considered main operating conditions do not show a major linear influence over the thermal time constant, demonstrating a relevant stability of the EH thermal response even when considering operation at partial load (in the range 1.5 to 5 MW_e). This outcome also confirms the flexibility of the unit and its adaptability to market requests. As expected, higher MS inlet temperatures lead to shorter τ, as highlighted by a correlation coefficient of about −0.42, due to a reduced impact of the thermal inertia opposed by the unit during the ramping up. The delay, δ, has a major dependency on the MS flow rate, as from its definition, and values in between 93 s and 173 s have been evaluated. The sum $\delta + \tau$ is primarily driven by the time constant, as shown by a correlation coefficient of 0.97. It presents dependencies with respect to the different working conditions similar to the ones showed for the time constant.

Fig. 12 also shows the influence of the main operating conditions, delay and time constant over the ramping up efficiency of the EH, as calculated after one- (MS outlet temperature at 63.2 % of its steady state value) and four-time (completed ramping up with MS outlet temperature above 98 % of its steady state value) constants. As expected, a strong linear correlation, about 0.7, is observed between $\eta^{\tau}_{ramp-up}$ and $\eta^{4\tau}_{ramp-up}$. Higher delays cause a reduction of the EH ramping up efficiency due to the losses occurring during the delay period in which limited MS temperature increase is observed. Longer thermal time constants promote an increase of the EH dynamic ramping up efficiency as calculated after one-time constant interval, $\eta^{\tau}_{ramp-up}$. Whilst it shows negligible influence when considering the operation over four-time constants. Longer τ leads to less steep MS outlet temperature profiles, thus smoother transitions and overall improved EH performance, at the expenses of slower responses and longer recirculation periods. Among the considered operating conditions the MS initial EH outlet temperature, $T^0_{EH,out}$, has the highest influence over the EH ramping up efficiencies with correlation coefficients of about 0.74 and 0.56 on $\eta^{\tau}_{ramp-up}$ and $\eta^{4\tau}_{ramp-up}$, respectively.

Fig. 13 further shows the dependency of $\eta^{\tau}_{ramp-up}$ (Fig. 13 (a)) and $\eta^{4\tau}_{ramp-up}$ (Fig. 13 (b)) on the MS initial temperature and it also presents (via the colour of the dots) the thermal time constant for the different tests. The linear fitting of the data is shown by the dashed lines and summarized in Table 9. The grey area around the linear fitting shows a range of confidence of ± 25 % and ± 10 % for $\eta^{\tau}_{ramp-up}$ and $\eta^{4\tau}_{ramp-up}$, respectively. The EH ramping up efficiency calculated after one time constant, $\eta^{\tau}_{ramp-up}$, presents lower values than $\eta^{4\tau}_{ramp-up}$ as it is more largely affected by both the delay and the thermal time constant. The thermal inertia of the equipment leads to efficiencies in the range 0.2–0.8. A steep increase is registered with increasing MS initial EH inlet temperatures, $T^0_{EH,in}$, as less heat is dispersed to counteract the system's thermal inertia. Additionally, higher initial MS temperature cause lower MS viscosity and lower viscosity changes during operation, thus promoting higher heat transfer coefficients and more uniform temperature distribution limiting stratification. When considering design MS EH inlet temperature and initial temperatures below 225 °C, an average $\eta^{\tau}_{ramp-up}$ of about 0.343 is measured.

The full EH ramping up efficiency calculated after four-time constants still presents a linear increase with the initial MS temperature. However, lower rate of efficiency increment with $T^0_{EH,in}$ and efficiency values generally closer to the design targets, in the range 0.7–0.95, are measured. The latter observation is expected as the influence of thermal inertia is exponentially reduced over time. Due to the reduced influence of both τ and δ, the spread of data for $\eta^{4\tau}_{ramp-up}$ is more limited than for $\eta^{\tau}_{ramp-up}$ as shown by the ±10 % range around the linear fitting (as opposed to the ±25 % shown for $\eta^{\tau}_{ramp-up}$). When considering design MS EH inlet temperature and initial temperatures below 225 °C, an average $\eta^{4\tau}_{ramp-up}$ of about 0.80 is measured. These results further confirm the potential of MS based power to heat units for frequency regulation as limited losses are faced and design efficiencies can be attained quickly.

Finally, Fig. 14 highlights the exponential dependency of the EH ramping up efficiency with the calculated thermal time constants. Fig. 14 also clarifies the efficiency increment reported in Fig. 13 between one- and four-time constant ramping up efficiencies. Overall, a steep efficiency increment is recorded already when considering a two-time constant interval. Further increments at progressively lower rates are visible in the full considered range up to eight-time constants interval. In average in the first four-time constants interval the EH ramping efficiency increases from about 0.53 to about 0.82. Whilst over the time

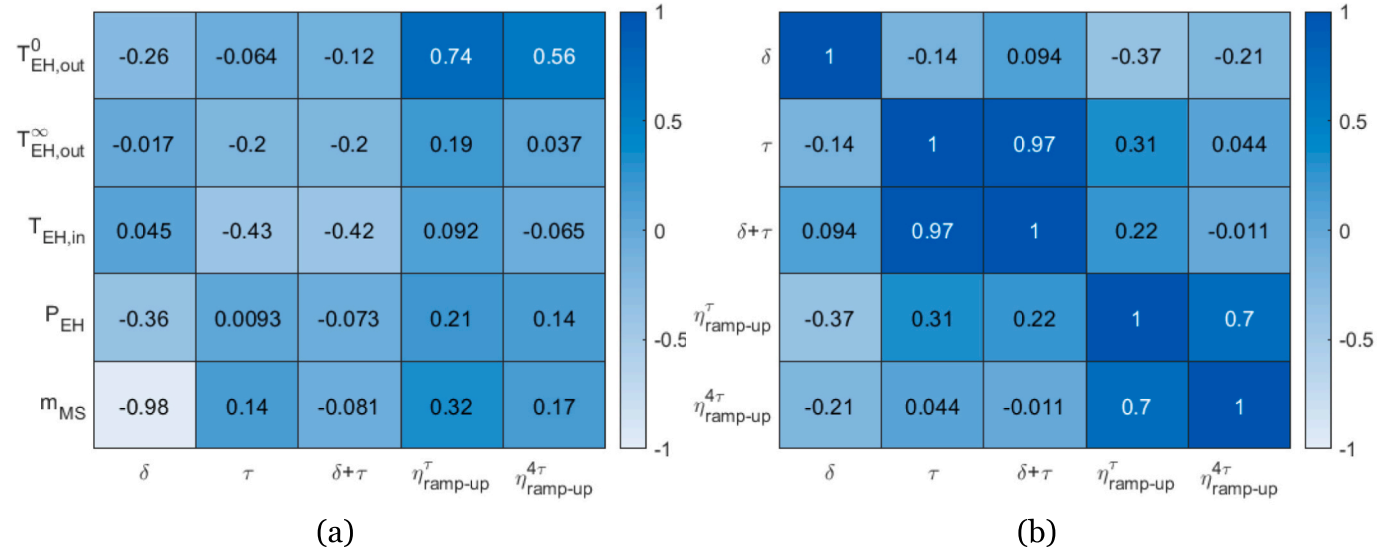

Fig. 12. (a) Correlation coefficients matrix for the main operational parameters and dynamic KPIs of the EH, (b) Correlation coefficients matrix among the dynamic KPIs of the EH.

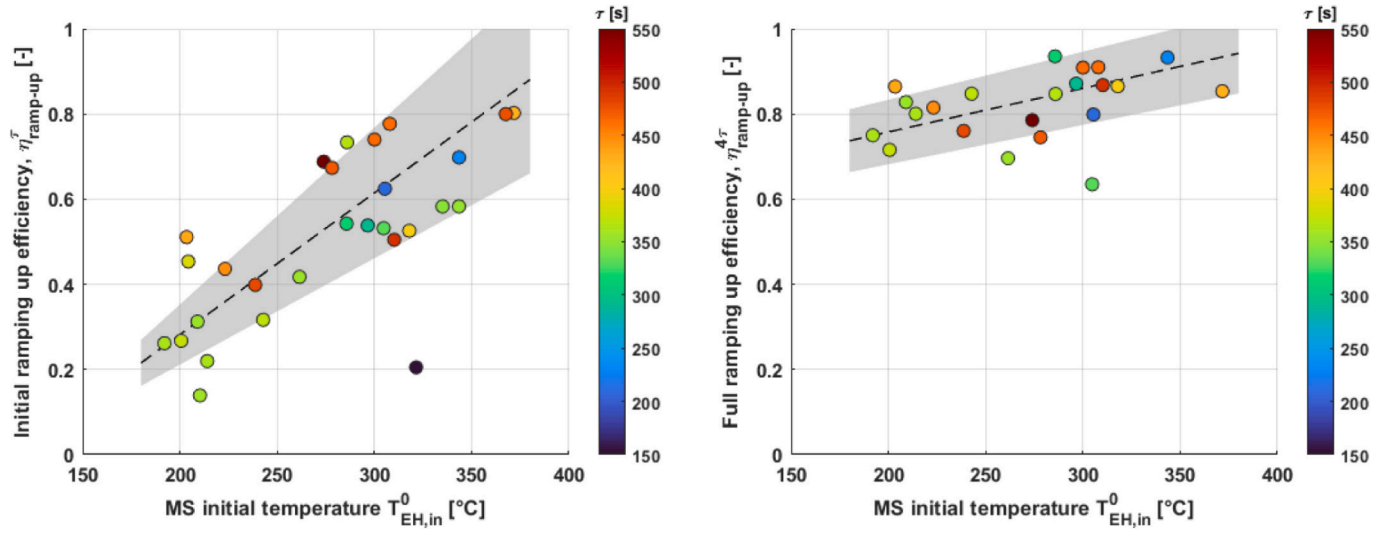

Fig. 13. Average EH ramping up efficiency during the start-up procedure against MS initial temperature and relative linear fitting of experimental data: (a) initial ramping up efficiency during the time interval [0-τ] s (and ± 25 % confidence range); (b) full ramping up efficiency during the time interval [0-4τ] s (and ± 10 % confidence range).

Table 9
Linear fitting for the average charge efficiency as calculated during t < τ and t < 4*τ.

Parameter	Linear fit	Unit
η^{τ}_{ch}	$0.003327 \cdot T[^{\circ}C] - 0.3833$	–
$\eta^{4\tau}_{ramp-up}$	$0.001026 \cdot T[^{\circ}C] - 0.5526$	–

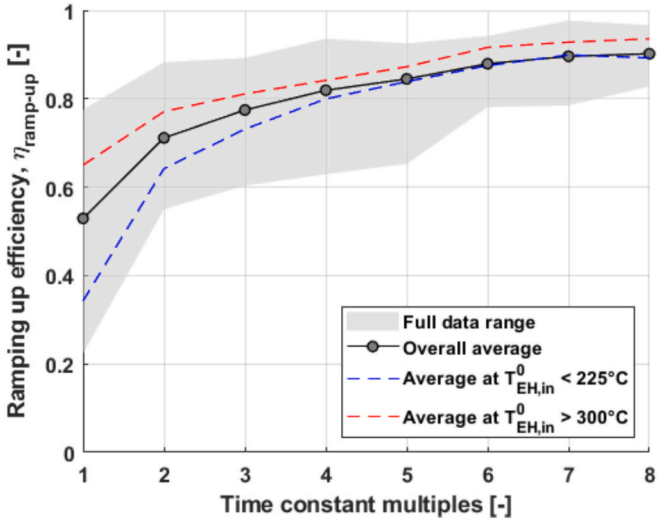

Fig. 14. Ramping up efficiency of the EH as calculated at different multiples of the unit's thermal time constant.

interval between four and eight-time constant the ramping efficiency increment is limited to about and addition 0.1. Additionally, for modelling purposes, the overall average ramping up efficiency can be approximated via a logarithmic function as $\eta^{x\tau}_{ramp-up} = 0.1755 \cdot \log(x) + 0.5619$, where x is the multiple of the thermal time constant.

The dashed lines report the ramping up efficiencies as calculated in the tests with initial MS temperature lower than 225 °C (close to the design conditions, blue curve) and higher than 300 °C (red curve). As from the previous considerations, higher MS initial temperatures oppose lower thermal inertia contributing to higher ramping up EH efficiencies. However, regardless of the MS initial temperature, it can be observed that after four-time constant the average ramping up efficiency is already within a range 0.82 ± 0.02. Considering even l0nger time intervals, the ramping efficiency gets closer to the design values above 0.90 and even lower variations are visible.

4. Conclusions

This study presents the thermal and dynamic performance of a MW scale power-to-heat unit integrating a ternary molten salts based TES for industrial heat decarbonization. Operational data, performance indicators, as well as specific curves measured during charge, discharge, and simultaneous operation of the full scale flexible power-to-heat system (5 MW_e, 18 MWh_{th}, 4 MW_{th}) are shown. Additionally, this study highlights the specific dynamic performance of the electric heater unit (5 MW_e), key components required to attain system's flexibility. Time constants and thermal responsiveness as well as efficiency during transient operation are presented and discussed.

From the discussed results the below main conclusions can be drawn:

- The investigated power-to-heat unit integrating a molten salts based TES presents stable operation both under design conditions as well as partial load conditions. Thus, flexible power-to-heat systems integrating a molten salts based TES represent a technically valuable and reliable solution for industrial decarbonization ensuring heat on demand.
- The unit can attain thermal round trip efficiencies above 94 % in near design operation with charge efficiency up to 98 % and discharge efficiency as high as 97.5 %. Limited efficiency reductions are visible in off-design operation with round trip values of about 90 %. These values confirm commercial targets for similar industrial power to heat installations, supporting their potential toward an effective industrial heat decarbonization.
- The salts working temperatures represent the most relevant working conditions affecting the off-design performance of the unit. To maintain elevated efficiency in part-load conditions it is suggested to act primarily on the salts flow rate and aim at maintaining the operating temperatures within a range ±20 % of the design values.

- A layered thermal insulation of about 100 mm can limit thermal losses from the tanks during standstill to about 0.5 °C/h and 2.3 °C/h in cold and hot conditions, respectively. The values are in line with expected lower losses when considering upscaled TES tanks. Cold standby should be prioritized over hot standby in operation as losses can be constrained within less than 6 °C during a standby cycle shorter than 12 h.
- The 5 MW_e power to heat system can attain full electric load in less than 90 s fulfilling the standard technical requirements for activation time for participation in the frequency restoration reserve markets. The electric heater can ramp up its electric power consumption from 0 to 5 MW_e in about 5 s. Thus, the unit can participate in frequency regulation markets untapping the potential for additional revenue streams.
- The electric heater unit is characterized by thermal time constants in the range 320–490 s, and by thermal efficiency during the full thermal ramping up process of about 80 % when considering design initial molten salts temperature below 225 °C. This guarantees reduced losses in flexible operation.
- Validated correlations for the dynamic thermal response of the electric heater are presented and discussed and they can be used in different dynamic modelling contexts to enhance accuracy and facilitate the integration of power to heat units in flexible grids.

This work provides the ground for further technological development and performance validation of similar large scale flexible power-to-heat systems. The dynamic characterization of the electric heater unit provides relevant insights to maximize the controllability of the unit and its integration in flexible grids, whilst providing specific data useful for dynamic modelling and integration assessment.

The elevated round trip efficiency, limited thermal losses and rapid activation times presented by the study suggest that relevant techno-economic performance can be attained by similar installations. More detailed investigations on the topic will be carried out as future work with a major focus on further upscaling as well as on the relevance of untapped business models thanks to the system participation in flexibility services. Additional future work will also focus on predictive operation and maintenance schemes to further optimize the unit's exploitation as well as on understanding the potential impact of salts properties evolution after long operation and multiple cycles.

CRediT authorship contribution statement

Silvia Trevisan: Writing – original draft, Visualization, Validation, Resources, Project administration, Methodology, Investigation, Funding acquisition, Formal analysis, Data curation, Conceptualization. **Sharat Pathi:** Writing – review & editing, Methodology. **James Brown:** Writing – review & editing, Methodology, Conceptualization. **Bjarke Buchbjerg:** Writing – review & editing, Conceptualization. **Andres Barros Borrero:** Writing – review & editing, Conceptualization. **Rafael Guedez:** Writing – review & editing, Project administration, Methodology, Funding acquisition, Conceptualization.

Declaration of competing interest

The authors declare that they have no known competing financial interests or personal relationships that could have appeared to influence the work reported in this paper.

Acknowledgement

This research has been funded by Kyoto Group AS through the research project "Renewable Industrial Heat On-Demand" (RIHOND) and it has also received funding from the European Union's Horizon Europe research and innovation programme under grant agreements No 101136000 (SCO2OP-TES) and No 101147078 (I-UPS).

Appendix

The below figure presents the validity of the derivation of the EH thermal time constant from the performed testing for two case studies operating the EH at full (5 MW_e – Fig. A1 (a)) and at partial load (3 MW_e – Fig. A1 (b)). The EH outlet temperature calculated as from Eq. (9), and its ±5 % error margin, are shown against the experimental measurements. The EH electric power is also shown highlighting the specific ramping. The experimental measurements are within the ±5 % error margin with larger deviation in the very initial stages of the EH ramping process which could still be attributed to the initial conditions and impossibility to attain a steeper EH power increase.

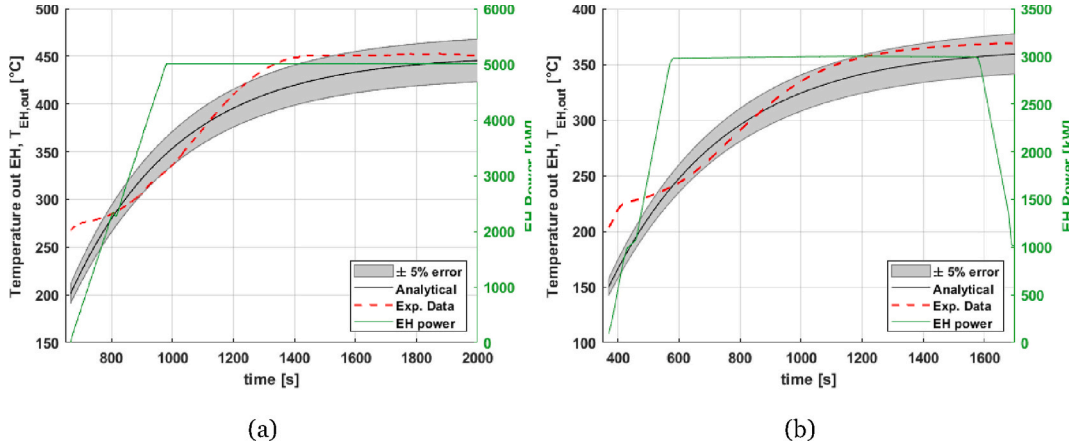

Fig. A1. MS electric heater outlet temperature as obtained from testing campaign (Exp. Data) and as from analytical approach including EH thermal time constant (as from Eq.) at full EH load (a) and at EH partial load (b).

Data availability

Data will be made available on request.

References

[1] Ritchie H, Roser M, Rosado P. CO_2 and Greenhouse Gas Emissions. Publ. online OurWorldInData.org [Online]; 2020. Available: https://ourworldindata.org/co2-and-other-greenhouse-gas-emissions.
[2] United Nations. *Paris Agreement*; 2015.
[3] IRENA. *Global Energy Transformation: A Roadmap to 2050*, Abu Dhabi; 2019.
[4] INTERNATIONAL ENERGY AGENCY. *Renewables 2023 Analysis and Forecast to 2028*; 2023.
[5] Marco A, Trevisan S, Matteucci F, Cabeza LF. Innovation trends on high-temperature thermal energy storage to defossilize energy systems. J Energy Storage 2024;103(PA):114261.
[6] Renewable Energy Agency I. *Renewable power generation costs in 2017 acknowledgements*; 2018.
[7] IRENA International Renewable Energy Agency. *Innovation Outlook: Thermal Energy Storage*, Abu Dhabi; 2020.
[8] Borg T, Christensen K, Lund H, Sorknæs P. The role of thermal energy storages in future smart energy systems. Energy 2024;313(June):133948.
[9] Madeddu S, Ueckerdt F, Pehl M, Peterseim J, Lord M, Kumar KA, et al. The CO2 Reduction potential for the European Industry via Direct Electrification of Heat Supply (Power-to-Heat). Environ. Res. Lett. 2020;15:124004.
[10] Sorknæs P, Johannsen RM, Korberg AD, Nielsen TB, Petersen UR, Mathiesen BV. Electrification of the industrial sector in 100 % renewable energy scenarios. Energy 2022;254:124339.
[11] Prenzel M, Klasing F, Kirschbaum S, Bauer T. Zero-emission chemical sites – combining power purchase agreements with thermal energy storage. J Energy Storage 2025;114(PB):115667.
[12] Pee A. de, Pinner D, Roelofsen O, Somers K, Speelman E, Witteveen M. *Decarbonization of Industrial Sectors: The next Frontier*; 2018.
[13] European Central Bank. Euro Foreign Exchange Reference Rate; 2022.
[14] Peng P, Yang L, Menon AK, Weger N, Prasher R, Breunig H, et al. *Techno-Economic Analysis of High-Temperature Thermal Energy Storage for On-Demand Heat and Power*; 2022.
[15] Trevisan S, Buchbjerg B, Guedez R. Power-to-heat for the industrial sector: techno-economic assessment of a molten salt-based solution. Energy Convers Manag 2022;272(October):116362.
[16] Royo P, Johnson M, David N, Fiss M, Ana ML. Experimental analysis of a power-to-heat storage with high-temperature phase change materials to increase flexibility and sector coupling 2024; **236**(October 2023).
[17] Xiao X, Jia H, Wen D, Golizadeh Y, Badiei A. Experimental Investigation of a Latent Heat Thermal Energy Storage Unit Encapsulated with Molten Salt / Metal Foam Composite Seeded with Nanoparticles 2023; **4**(May 2021): 74–85.
[18] Weiss J, Hübner F, Fluri T. Experimental characterisation of a molten salt thermal energy storage with filler. J Energy Storage 2024;103(PB):114420.
[19] Osorio JD, Mehos M, Imponenti L, Kelly B, Price H, Torres-Madronero J, et al. *Failure analysis for molten salt thermal energy storage tanks for in-service CSP plants*; 2024.
[20] Mahdi Z, Merige PS, Chico Caminos RA, Schmitz P, Herrmann U, Teixeira Boura C, et al. Modeling the thermal behavior of solar salt in electrical resistance heaters for the application in PV-CSP hybrid power plants. *Proceedings of the SOLARPACES 2020: 26th international conference on concentrating solar power and chemical energy systems*. 2022.
[21] Yang Y, Yuan X, Li Z, He L. Conceptual design of eccentric micro annular channel electric heater for a thermal energy storage system. J Energy Storage 2024;99(PA):113191.
[22] Rosatos P, Itskos G, Nikolopoulos N. Cross-cutting CFD support for efficient design of a molten salt electric heater for flexible concentrating solar power plants. Energies 2023;16(6403).
[23] He X, Wang Y, Ren C, Yu L, Hu N, Zheng C. Mitigation of the local overheating phenomenon in molten salt electric heaters through flow field optimization. J Energy Storage 2024;94(May):112229.
[24] Prenzel M, Bauer T, Kamnang W, Fernholz B, Stengler J. Performance testing of two 360 KW electric hetares for molten salts. (October); 2023.
[25] Prenzel M, Bauer T, Kamnang W, Fernholz B, Stengler J. Molten salt electric heaters: lessons learned from DLR ' s TESIS facility and intensive prototype testing M; 2024. p. 1–13.
[26] Bhatnagar P, Siddiqui S, Sreedhar I, Parameshwaran R. Molten Salts: potential candidates for thermal energy storage applications. Int J Energy Res 2022;July:17755–85.
[27] Honkapuro S, Riikonen J, Price A. Role of power-to-heat and thermal energy storage in decarbonization of district heating. Energy 2024;305(December 2023).
[28] Iov F, Khatibi M, Bendtsen JD. On the participation of power-to-heat assets in frequency regulation markets — a danish case study. Energies 2020;13.
[29] Yara International ASA. Yara MOST [Online]; 2022. Available: https://www.yara.com/chemical-and-environmental-solutions/solar-power-molten-salt/.
[30] Zavoico AB. *Solar power tower design basis document revision 0;* 2001.
[31] "ENERGINET" [Online]. Available: https://en.energinet.dk/. [Accessed: 16-Dec-2024].
[32] Hey JE, Hodson SL, Yazawa K, Doty J, Fisher TS. Experimental characterization of dynamic heat exchanger behavior. Int J Heat Mass Transf 2018;121:933–42.
[33] Jiang K, Zhang G, Liu H, Mu Z, Wang Q, Qin T, et al. Design and dynamic simulation of flue gas-molten salt heat exchanger in flexible operation coal-fired power plant. J Energy Storage 2024;93(May):112227.
[34] Skogestad S. *Chemical and energy process engineering*; 2009.
[35] Tagle-salazar PD, Prieto C, Anton L. A transient heat losses model for two-tank storage systems with molten salts **219**(April); 2023.
[36] Zhang X, Wu Y, Ma C, Meng Q, Hu X, Yang C. Experimental study on temperature distribution and heat losses of a molten salt heat storage tank; 2019.
[37] ENTSO-E. Automatic frequency restoration reserve process; 2024.
[38] Schmidt O, Melchior S, Hawkes A, Staffell I. Projecting the future levelized cost of electricity storage technologies. Joule 2019;3(1):81–100.